Biodegradable Biliverdin Nanoparticles for Efficient Photoacoustic Imaging

*Parinaz Fathi [1, 2, 3], Hailey J. Knox [4], Dinabandhu Sar [1,2], Indu Tripathi [1, 2], Santosh K. Misra [1, 2], Fatemeh Ostadhossein [1, 2], Mandy B. Esch [3], Jefferson Chan [4, *], Dipanjan Pan [1, 2, *]*

[1] Departments of Bioengineering, Materials Science and Engineering, and Beckman Institute, University of Illinois, Urbana, IL 61801 United States

[2] Mills Breast Cancer Institute, Carle Foundation Hospital, Urbana, IL 61801, United States

[3] Biomedical Technologies Group, Microsystems and Nanotechnology Division, Physical Measurement Laboratory, National Institute of Standards and Technology, Gaithersburg, MD 20899 United States

[4] Department of Chemistry and Beckman Institute, University of Illinois, Urbana, IL 61801, United States

ABSTRACT. Photoacoustic imaging has emerged as a promising imaging platform with a high tissue penetration depth. However, biodegradable nanoparticles, especially those for photoacoustic imaging, are rare and limited to a few polymeric agents. The development of such nanoparticles holds great promise for clinically translatable diagnostic imaging with high biocompatibility. Metabolically digestible and inherently photoacoustic imaging probes can be developed from nanoprecipitation of biliverdin, a naturally occurring heme-based pigment. The synthesis of nanoparticles composed of a biliverdin network, cross-linked with a bifunctional amine linker, is achieved where spectral tuning relies on the choice of reaction media. Nanoparticles synthesized in water or water containing sodium chloride exhibit higher absorbance and lower fluorescence compared to nanoparticles synthesized in 2-(*N*-morpholino) ethane sulfonic acid (MES) buffer. All nanoparticles display high absorbance at 365 nm and 680 nm. Excitation at near-infrared wavelengths leads to a strong photoacoustic signal, while excitation with ultraviolet wavelengths results in fluorescence emission. *In vivo* photoacoustic imaging experiments in mice demonstrated that the nanoparticles accumulate in lymph nodes, highlighting their potential utility as photoacoustic agents for sentinel lymph node detection. The biotransformation of these agents was studied using mass spectroscopy and they were found to be completely biodegraded in the presence of biliverdin reductase, a ubiquitous enzyme found in the body. Degradation of these particles was also confirmed *in vivo*. Thus, the nanoparticles developed here are a promising platform for biocompatible biological imaging due to their inherent photoacoustic and fluorescent properties, as well as their complete metabolic digestion.

KEYWORDS. biliverdin, biodegradation, bioimaging, fluorescent, nanoparticle, nanoprecipitation, photoacoustic

Photoacoustic (PA) imaging is a technique that combines optical excitation with ultrasound detection to achieve superior depth of penetration compared to fluorescence imaging.[1] Nanoparticle-based imaging probes have been utilized as an alternative to small-molecule probes due to advantages such as the ability to tune their surface characteristics, increase circulation time, and target tissues of interest. Nanoparticles with photoacoustic properties[2,3,12–15,4–11] are a class of contrast agents that hold great potential for multiscale diagnostic applications.[16–21] However, a majority of these nanoparticles are based on polymeric or metallic designs and therefore may remain in the body for extended time periods. In fact, 30-99% of nanoparticles will accumulate in the liver,[22] and a variety of nanoparticles have been shown to negatively impact liver cells.[23–29] With the exception of a few classes (*e.g.* iron oxide), only several examples of nanoparticles have been translated to a clinical setting.[30–35] One of the key determinants that would improve translational potential of nanoparticles is to improve their biodegradation profile. Specifically, there is a need for the development of photoacoustic nanoparticles that can be degraded in the body after the imaging session has been performed. The goal of the present work is to utilize endogenous molecules for designing inherently photoacoustic nanoparticles that, at the same time, could offer a solution to the issue of biodegradation.

In order to develop biodegradable nanoparticles with inherent photoacoustic imaging capabilities, we proposed the use of biliverdin, a water-soluble, naturally-occurring bile pigment that results from the breakdown of heme.[36] During this process, biliverdin is reduced to water-insoluble bilirubin through the action of an enzyme, biliverdin reductase.[36–38] The inherent breakdown pathway of biliverdin led us to hypothesize that nanoparticles composed of biliverdin would be entirely biodegradable *in vivo*. Biliverdin has two main absorbance bands; one between 350 nm and 400 nm, and the other between 600 nm and 700 nm.[39] The absorbance above 650 nm

is important for *in vivo* applications because interference from the surrounding tissue is minimal between 650-900 nm (*i.e.*, the first biological imaging window).[40]

Many photoacoustic nanoparticles obtain their photoacoustic properties through the incorporation of dyes or metals,[6,7,10,15] rather than through selection of intrinsically photoacoustic building blocks. These approaches pose a challenge due to the potential for toxicity of the metals, or premature release of the incorporated dyes. There are very few examples reported in the literature of nanoparticles derived entirely from endogenous species. For instance, a recent report revealed the synthesis of cisplatin-chelated bilirubin nanoparticles for photoacoustic imaging and photothermal therapy.[41] An important distinction is that while biliverdin has strong absorbance in the near-infrared region, bilirubin does not. Thus, in order for bilirubin-based nanoparticles to exhibit their favorable photoacoustic properties, it was necessary for cisplatin, a xenobiotic metal-based anti-cancer drug, to be incorporated. Additionally, the enzymatic degradation of these nanoparticles has not been reported

Here we report the synthesis of fully biodegradable nanoparticles that do not require the chelation of metals to exhibit photoacoustic properties suitable for *in vivo* imaging. Importantly, we expand the utility of these nanoparticles further by leveraging the blue-shifted absorbance for fluorescence imaging. The utility of these nanoparticles for bioimaging was demonstrated through application as a sentinel lymph node imaging probe. Finally, we demonstrate that the nanoparticles can be completely degraded both *in vitro* and *in vivo* by biliverdin reductase, an enzyme present throughout the body, and especially in the liver.[37,42]

RESULTS & DISCUSSION.

Synthesis. To develop biliverdin nanoparticles (BVNPs), biliverdin hydrochloride ($C_{33}H_{34}N_4O_6$ •HCl) was nano-precipitated using stoichiometric amounts of 1-ethyl-3-(3-dimethylaminopropyl) carbodiimide (EDC) and 2,2' ethylenedioxy bis(ethylamine) (henceforth referred to as diamine). The products obtained from this reaction were found to be highly dependent on the nature of the reaction media. We conducted the reactions in water, in 0.1 M 2-(*N*-morpholino) ethanesulfonic acid (MES) buffer, and in 0.15 M aqueous NaCl solution. The resultant BVNPs are designated water-BVNPs, MES-BVNPs, and NaCl-BVNPs, respectively (Scheme 1).

The sizes of the nanoparticles were determined using transmission electron microscopy (TEM). We found that the addition of EDC, *N*-hydroxysuccinimide (NHS), and diamine to biliverdin dissolved in water led to the formation of small nanoparticles with an average diameter of 2.3 nm at 10 min, and larger nanoparticles with an average diameter of 105 nm when the components were allowed to react for 24 h (Figure 1A). Water-BVNPs and NaCl-BVNPs showed an immediate color change upon addition of the diamine, while the color of the MES-BVNPs remained unchanged. The absorbance peaks of the BVNPs was markedly different with respect to free biliverdin, indicating successful particle self-assembly (Figure 1B). The synthesis that was conducted in the NaCl solution exhibited similar absorbance characteristics to that of water-BVNPs (Figure 1B) and resulted in spherical nanoparticles with an average diameter of 14.2 nm after 24 h (Figure 1A). In contrast, when the synthesis was performed in MES buffer, nanoparticles with diameters of 26.5 nm and 43.8 nm were observed at the 10-min and 24-h time points, respectively (Figure 1A). These particles did not show a significant change in size when the reaction time was extended, indicating that the reaction in MES was controlled and had formed stable particles.

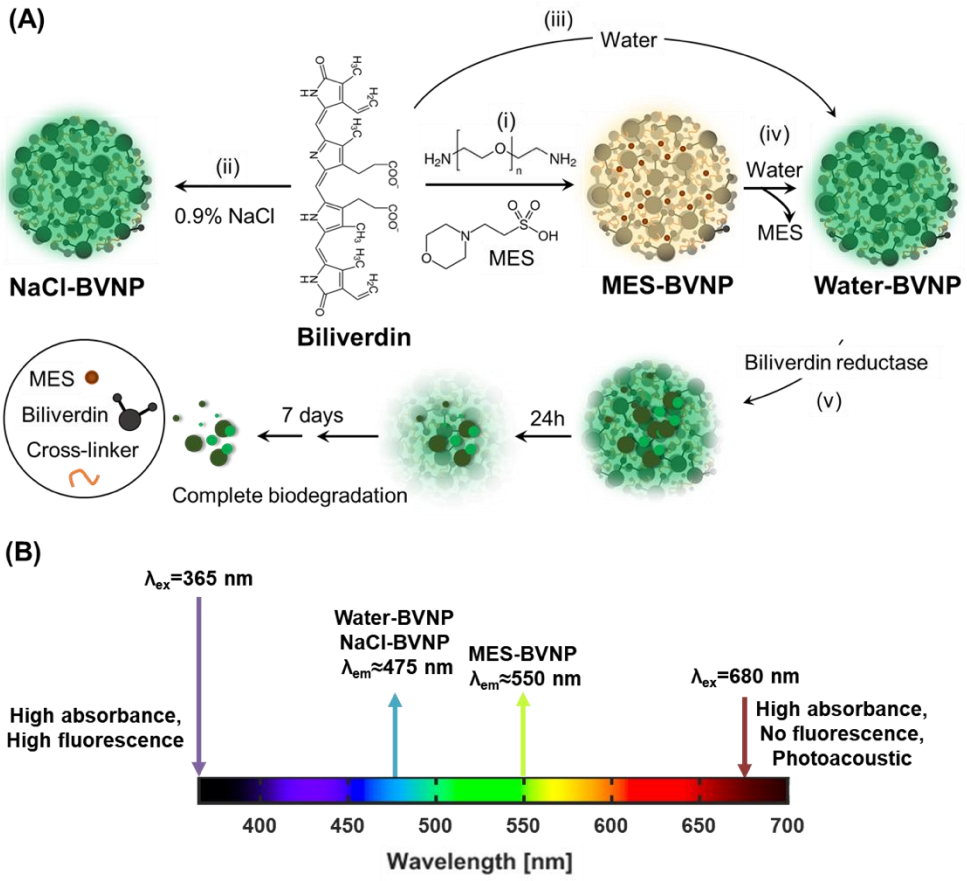

Scheme 1. (A) BVNP synthesis schematic. The synthesis solvent determines BVNP composition and spectral properties. The use of water, MES, and NaCl results in water-BVNPs **(iii)**, MES-BVNPs **(i)**, and NaCl-BVNPs **(ii),** respectively. Dialysis of MES-BVNPs with water **(iv)** results in water-BVNPs. Nanoparticles degrade in the presence of biliverdin reductase **(v)**. **(B)** MES-BVNPs have a red-shifted fluorescence compared to the Water-BVNPs and NaCl-BVNPs. All compositions exhibit high absorbance at 365 nm and 680 nm, resulting in fluorescent and photoacoustic properties respectively.

Photophysical Characterization. The photophysical properties of the nanoparticles were characterized using a full suite of techniques including UV-Vis spectroscopy, Fourier transform infrared spectroscopy (FT-IR), mass spectrometry, zeta potential measurements, fluorescence spectroscopy, fluorescence imaging, and photoacoustic tomography. The MES-BVNPs showed a broadening of the UV-Vis peak at ≈650 nm, as well as a decrease in overall absorbance at all wavelengths compared to water-BVNPs and NaCl-BVNPs (Figure 1B).

FT-IR spectroscopy (Figure 1C, Figure S1) revealed that the crosslinker had peaks at 1585 cm^{-1} (peak 1, N-H bend), 1305 cm^{-1} (peak 2, C-N stretch), and 1130 cm^{-1} (peak 3, C-N stretch). Unincorporated biliverdin had C-N stretches at 1330 cm^{-1} (peak 6), 1305 cm^{-1} (peak 2), 1280 cm^{-1} (peak 7), 1260 cm^{-1} (peak 8), and 1120 cm^{-1} (peak 9). The formation of amide bonds as a result of EDC-NHS crosslinking was confirmed by the appearance of peaks at 1678 and 1653 cm^{-1} (peaks 10 and 11) for the BVNPs. MES-BVNPs exhibited a unique set of peaks in the range of 800 cm^{-1} -1500 cm^{-1} compared to the water-BVNPs and the NaCl-BVNPs. The sharp peak near 1030 cm^{-1} (peak 12) can be attributed to the S=O in MES,[43] while the peak near 910 cm^{-1} (peak 13) can be attributed to the S-OH bond in MES, indicating that it is plausible that MES molecules were entrapped within the nanoparticle. 24 h MES-BVNPs dialyzed with MES retained the peaks at 1030 cm^{-1} and 910 cm^{-1}, while 24 h MES-BVNPs dialyzed with water no longer had these peaks, indicating that dialysis with water led to the removal of MES from the particles (Figure S1 B). All three nanoparticle types were found to have negative zeta potentials, with no statistically significant difference in zeta potential between the 10-min and 24-h time points for any of the types (Figure 1D). The reduction in zeta potential magnitude of 24-h MES-BVNPs compared to 24-h water-BVNPs further suggests a relationship between the reaction media and nanoprecipitation.

When the 10-min and 24-h samples were excited at 365 nm, all three nanoparticle types were fluorescent (Figure 2A). However, the MES-BVNPs showed the highest fluorescence, with a maximum intensity over ten-fold greater than that of the water-BVNPs and NaCl-BVNPs. This finding prompted us to determine the possible influence of MES. We dialyzed 10-min MES-BVNPs and water-BVNPs with water using dialysis cassettes with a size cutoff of 10 kDa. We hypothesized that if MES was influencing the photophysical properties, a greater change in MES-

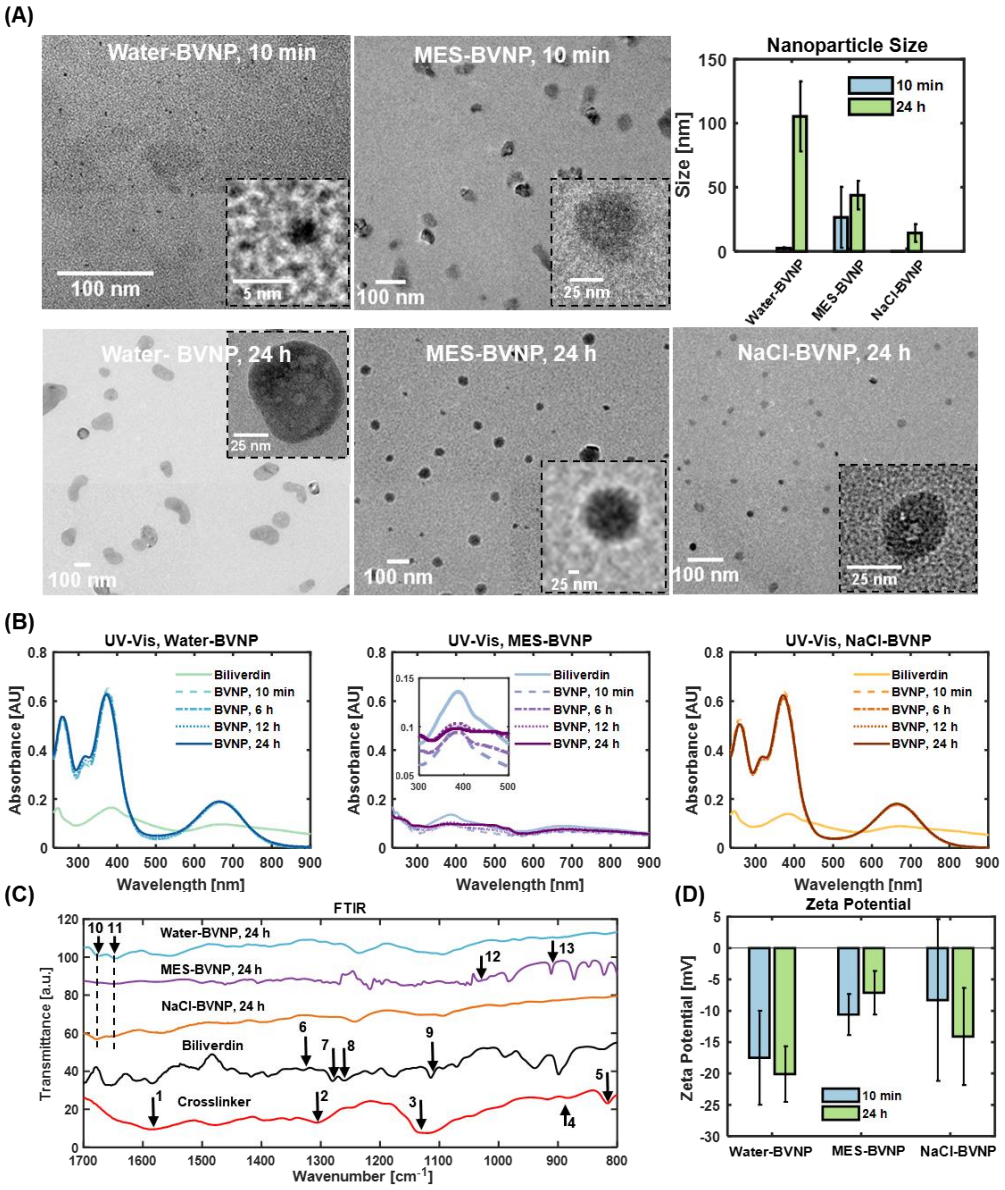

Figure 1. Physicochemical characterization of BVNPs. **(A)** TEM micrographs of different BVNP compositions. Spherical nanoparticles were found to be formed for each composition. Size was determined using ImageJ, and error bars represent standard deviation across all nanoparticles in a representative image for each nanoparticle type. **(B)** UV-Vis spectra for BVNPs. Water-BVNPs and NaCl-BVNPs display higher absorbance than MES-BVNPs. High absorbance is observed near 365 nm and 680 nm. **(C)** FT-IR spectra confirms the presence of differences between MES-BVNPs and other compositions, with peaks resulting from MES. **(D)** Zeta potential measurements indicate no significant zeta potential differences between Water-BVNPs, MES-BVNPs, and NaCl-BVNPs. Error bars represent standard deviation across twelve or more runs as automatically determined by the Malvern Zeta sizer software.

BVNP fluorescence would be observed compared to that of the water-BVNPs, which served as a control. Indeed, we found a larger fluorescence intensity fold change for the MES-BVNPs after dialysis with water. This suggested to us that the entrapped MES molecules were inducing a change in the fluorescence properties. Upon dialysis with water, the MES molecules were unloaded, resulting in a decreased fluorescence. Another interesting property is that the emission wavelength changed as a function of reaction time for the MES-BVNPs but not the Water-BVNPs and NaCl-BVNPs. In particular, the MES-BVNPs emission changed from blue (10-min) to yellow-green (24-h). The difference in fluorescence emission based on synthesis solvent was also observed under a 365 nm UV lamp for 24-h samples (Figure 2A). When observed under the UV lamp, MES alone did not exhibit any fluorescence (Figure S2). This finding suggests that it is possible to fine tune spectral properties of biliverdin nanoparticles through careful selection of the reaction media and synthesis time.

When excited at 680 nm, none of the three nanoparticle types exhibited fluorescence. A Spectrum *In vivo* Imaging System (IVIS) was used to perform further fluorescence imaging experiments (Figure 2B, Figure S2). The MES-BVNPs showed greater radiant efficiency than the other nanoparticle types and exhibited some fluorescence in the near-IR region for excitation wavelengths of 430 nm, 465 nm, and 500 nm. In all cases, the BVNPs showed no fluorescence at an excitation wavelength of 675 nm.

We conducted further experiments with multiple time-points between 10 min and 24 h to investigate MES-BVNP fluorescence change with synthesis time. For 365 nm excitation (Figure 2C), fluorescence intensity dropped between 10 min and 5 h. At 5 h the appearance of a second red-shifted peak is observed. By 10 h, the 2nd peak becomes more prominent than the first peak. The intensity then increases with time until 24 h, at which point it is the same intensity as that of

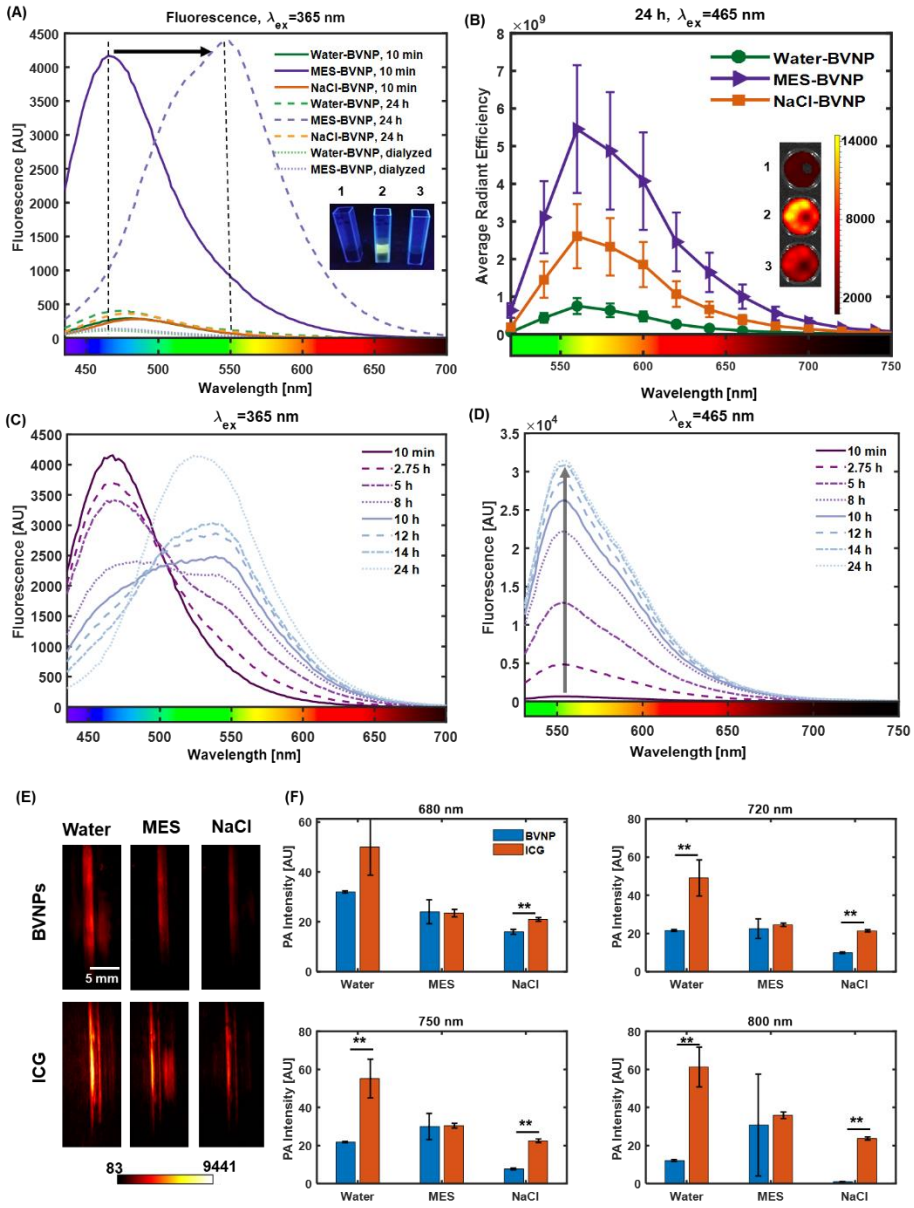

Figure 2. Spectral properties of BVNPs. **(A)** Fluorescence spectra for an excitation wavelength of 365 nm. MES-BVNPs exhibit red-shifting fluorescence with time, resulting in yellow-green fluorescence at 24 h. MES-BVNPs have the greatest fluorescence intensity. MES-BVNPs dialyzed with water lose their fluorescence advantage. Inset depicts 24-h BVNPs under a 365 nm lamp. 1, 2, and 3 correspond to Water-BVNP, MES-BVNP, and NaCl-BVNP respectively **(B)** Average Radiant efficiency for 24-h BVNPs at an excitation wavelength of 465 nm. MES-BVNPs were found to have higher radiant efficiency than Water-BVNPs and NaCl-BVNPs. Inset depicts IVIS image of BVNPs for an excitation wavelength of 500 nm and an emission wavelength of 680 nm. 1, 2, and 3 correspond to Water-BVNP, MES-BVNP, and NaCl-BVNP respectively. **(C)** MES-BVNP fluorescence change with time for an excitation wavelength of 365 nm. A decrease in fluorescence intensity is observed, followed by a fluorescence red-shifting and subsequent increase in fluorescence intensity to its initial magnitude. **(D)** MES-BVNP fluorescence change with time for an excitation wavelength of 465 nm. A steady increase in fluorescence intensity is observed with synthesis time. **(E)** Photoacoustic tissue phantom imaging of dialyzed BVNPs, compared to ICG dissolved in water at the same concentration. ICG concentrations were 0.51 mg/mL, 0.93 mg/mL, and 0.31 mg/mL respectively. An excitation wavelength of 680 nm was used. **(F)** ROI quantification of photoacoustic tissue phantom images. ** indicates statistical significance with $P<0.05$.

the 10 min particles. The results suggest that the MES-BVNP synthesis takes place in two distinct steps. Over the first 10 min, nanoparticles are formed. Over time, the fluorescence of these nanoparticles is quenched and then slowly red-shifts until it regains its fluorescence intensity. For 465 nm excitation (Figure 2D), fluorescence intensity increased with synthesis time. These behaviors are likely due to pi-pi stacking of the biliverdin molecules and their aggregation under the influence of MES, although further elucidation of this mechanism is beyond the scope of this work.

The high absorbance and lack of fluorescence upon excitation at 680 nm was exploited for photoacoustic imaging. Tissue phantoms for photoacoustic imaging were prepared as previously reported[44], and the protocol is briefly described in the Methods section. Images of tissue phantoms and example ROIs are provided in Figure S3. Photoacoustic images of dialyzed BVNPs in a tissue phantom were acquired, and compared to the reference dye indocyanine green (ICG) dissolved in water at the same final mass concentration (Figure 2E). ROI analysis in ImageJ was used to quantify the average photoacoustic intensity of each sample (Figure 2F). MES-BVNPs were found to have a comparable photoacoustic intensity to ICG at the same concentration for excitation wavelengths of 680 nm, 720 nm, 750 nm, and 800 nm. These results suggest that BVNP imaging performance is comparable to that of ICG, and BVNPs may be used as a nanoparticle-based alternative to ICG, which has been known to elicit adverse events such as allergic reactions[45,46]. The use of a biliverdin-based nanoparticle may reduce the occurrence of such reactions as biliverdin should not be recognized by the immune system as a foreign antigen. Statistical comparisons of photoacoustic intensity between the different types of BVNPs were not conducted as the final concentration of biliverdin in each type of particle will have a direct impact on the PA signal intensity. Additionally, our findings agree with previous reports that PA intensity is not

necessarily directly correlated with absorption and fluorescence spectra.[47] The mechanisms behind this behavior are not well-understood, but nonradiative deactivation, triplet state contribution, and photobleaching are believed to contribute to this behavior.[47–49] Further tissue phantom imaging experiments were conducted to determine the effects of synthesis time on photoacoustic signal intensity (Figure S4). These experiments demonstrated that water-BVNP and NaCl-BVNP photoacoustic intensity increased with synthesis time, while MES-BVNP photoacoustic intensity did not significantly change with synthesis time.

Hydrodynamic Size and Particle Concentration. Nanoparticle hydrodynamic size, particle concentration, and size distributions were determined using a Malvern Panalytical NanoSight NS300, which records videos of nanoparticles under flow. 10 1-minute videos were recorded for dialyzed 24 h water-BVNPs, MES-BVNPs, and NaCl-BVNPs. All BVNP types were found to have a high concentration of particles at or below 100 nm in size (Figure 3A) with some peaks at higher sizes, which potentially results from the formation of aggregates composed of multiple nanoparticles. D10, D50, and D90 values indicate that on average 10% of particles in each particle population (water-BVNPs, MES-BVNPs, and NaCl-BVNPs) are below 70 nm in size, 50% are below 100 nm in size, and 90% are below 200 nm in size (Figure 3B). The average hydrodynamic size of all three nanoparticle types was approximately 100 nm (Figure 3C), with no significant difference in size between the particle types. This is in contrast to the different nanoparticle anhydrous sizes as determined by TEM imaging, suggesting a relationship between the dialysis solvent and the hydration layer around the nanoparticles. NaCl-BVNPs have the smallest anhydrous nanoparticle size, while Water-BVNPs have the largest anhydrous nanoparticle size, indicating that water may lead to the formation of a smaller hydration layer around the

nanoparticles compared to MES buffer or NaCl solution. The mode nanoparticle size detected

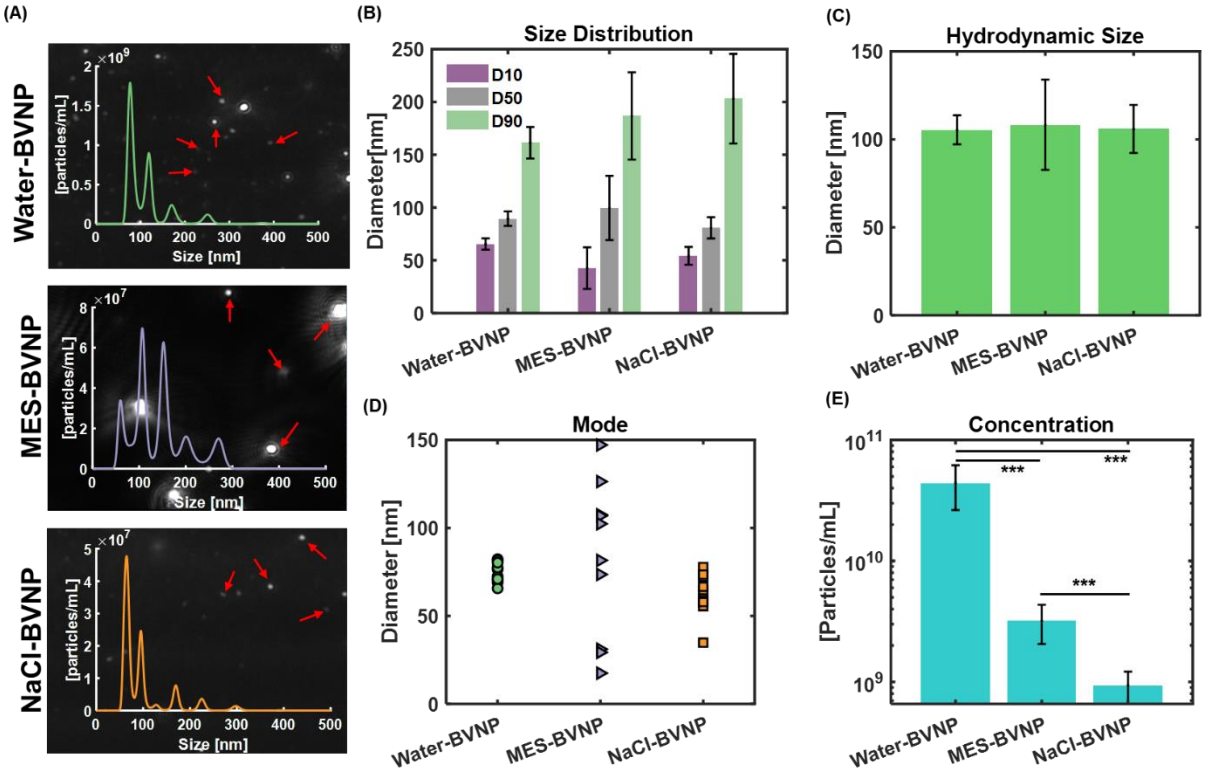

Figure 3. Nanoparticle Hydrodynamic size. (A) Screenshots from videos collected by Nanosight for size analysis. Red arrows point to some examples of nanoparticles. Overlays depict representative nanoparticle size distributions (concentration vs. size). **(B)** Hydrodynamic size distribution. 10% of detected nanoparticles are have sizes below the D10 value, 50% of detected nanoparticles are have sizes below the D50 value, and 90% of detected nanoparticles are have sizes below the D90 value. **(C)** Average hydrodynamic size for each type of particle. **(D)** The mode nanoparticle size (nanoparticle size with highest frequency of occurrence) for each type of particle. Each mode is calculated from one 1-minute Nanosight video. **(E)** Nanoparticle concentration post-dialysis, as determined by Nanosight video analysis. *** indicates statistical significance with $P<0.001$.

across 10 videos for each nanoparticle type was found to typically fall between 50 and 100 nm for Water-BVNPs and NaCl-BVNPs (Figure 3D). The concentration of nanoparticles per mL of final dialyzed particle solution was also determined (Figure 3E), with water-BVNPs having an average final concentration of 4.41 x 10^{10} particles per mL, MES-BVNPs having an average final concentration of 3.20 x 10^{9} particles per mL, and NaCl-BVNPs having an average final

concentration of 9.37 x 10^8 particles per mL. Since the final amount of biliverdin in each particle was determined as described in the previous section, this information was combined with the nanoparticle concentration to determine the number of biliverdin molecules in each particle. A detailed explanation of the calculations is provided in the Methods section. We determined that Water-BVNPs had an average of 1.196 x 10^7 biliverdin molecules per particle, MES-BVNPs had an average of 3.002 x 10^8 biliverdin molecules per particle, and NaCl-BVNPs had an average of 3.420 x 10^8 biliverdin molecules per particle. This suggests that the EDC-NHS reaction kinetics may differ based on the synthesis solvent, which leads to the formation of greater or fewer particles with greater or fewer biliverdin molecules incorporated in each particle.

Biocompatibility. Blood smear experiments and 3-(4,5-dimethylthiazol-2-yl)-2,5-diphenyltetrazolium bromide (MTT) cell viability assays were utilized to assess BVNP biocompatibility. For blood smear experiments, samples of whole pig blood were exposed to BVNPs (10% by volume) for 30 min, after which the blood was imaged using an optical microscope. Observation of morphological changes in nanoparticle-treated samples compared to an untreated control would indicate potential adverse reactions to the nanoparticles. No morphological changes were observed in nanoparticle-treated samples compared to the control, indicating a lack of adverse interactions between the nanoparticles and blood cells (Figure S5 A).

MTT experiments were separately conducted on MCF-7 cells, a metastatic breast cancer cell line, and MDA-MB-231 cells, a triple-negative metastatic breast cancer cell line. We chose these cells because breast cancer is a type of cancer that metastasizes to lymph nodes. We reasoned that in sentinel lymph node biopsies, the nanoparticles would first be injected at the tumor site, after which they would drain into the surrounding lymph nodes. MTT experiments were conducted with nanoparticle concentrations of 5 % and 10 % by volume for 10 min and 24 h water-BVNPs,

MES-BVNPs, and NaCl-BVNPs. Particle-treated cells typically had comparable or greater viability than untreated control cells (Figure S5 B, Figure S5 C). The increase in viability compared to control cells may indicate increased metabolic activity of cells exposed to the BVNPs, rather than an increase in cell proliferation.

***In vivo* Photoacoustic Imaging & *Ex vivo* Fluorescence Imaging.** To evaluate the feasibility of using these BVNPs as a diagnostic imaging probe for the lymphatic system, experiments were performed in live mice. Four groups of mice were administered water-BVNPs, MES-BVNPs, NaCl-BVNPs or a vehicle control *via* hock injection in the hindlimb. No adverse reactions were observed in the tissue from injection of the nanoparticles. Mice were imaged at 5, 10, 15, and 30 min post-injection, using 680 nm, 720 nm, and 750 nm excitation. *In vivo* photoacoustic imaging at 680 nm (Figure 4), 720 nm (Figure S6), and 750 nm (Figure S7) showed a marked increase in the signal as a result of nanoparticle injection. Importantly, all three nanoparticle types showed passive accumulation in the lymph nodes.[16,50–52] This was confirmed using *ex vivo* tissue analysis (*vide infra*). The PA signal intensity was also found to vary with time, indicating a time-dependent nanoparticle uptake within, and clearance from, the lymphatic system.

Following euthanization, the major organs were collected from the animals and photoacoustic imaging was performed to visualize the heart, lung, liver, kidneys, spleen, and lymph nodes. Our analysis indicated some nanoparticle accumulation in the liver and spleen. There was also some accumulation in the lymph nodes, but consistent with our *in vivo* experiments, the particles appeared to have mostly cleared from the lymphatic system 30 minutes post-injection (Figure 5A). These findings were further corroborated using fluorescence imaging of the various organs (Figure 5B). The organs dissected from nanoparticle-treated animals exhibited higher signal overall compared to the control water-treated animal, indicating the distribution of BVNPs

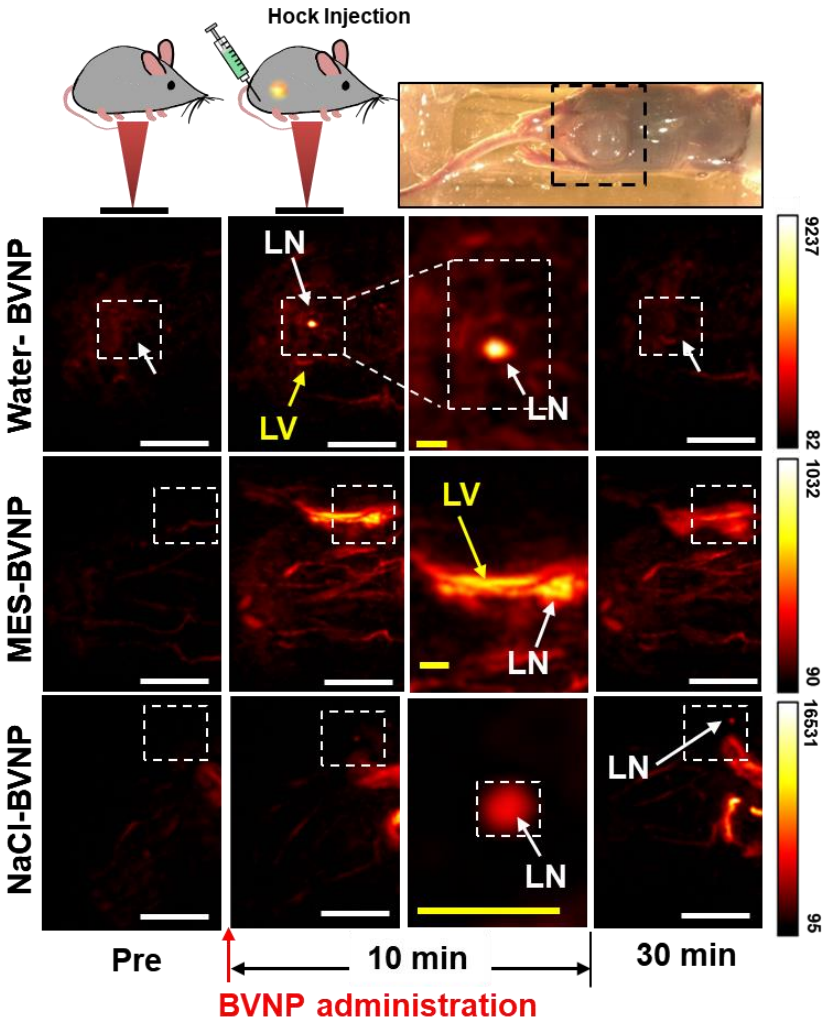

Figure 4. Photoacoustic Imaging of sentinel lymph nodes using BVNPs. 680 nm wavelength photoacoustic images of mice before nanoparticle injection, 10 min after injection, and 30 min after injection. An increase in PA signal intensity is observed post-injection, and nonspecific accumulation of BVNPs can be observed in lymph nodes. White scale bars represent 5 mm, and yellow scale bars represent 1 mm. LN=lymph node; LV= lymphatic vessel.

throughout the body. As in any *in vivo* experiment, biological variability from one animal to another likely played a role in this result. The high error bar in MES-BVNP lymph nodes suggests that the particles may have taken greater than 30 minutes to clear from the lymphatic system in some of the mice. Since the animals were sacrificed 30 min post-injection, these particles may not have fully cleared from the lymphatic system by then, and this in turn led to a high error bar in the

fluorescence signal quantification. The ability of these nanoparticles to be detected with fluorescence imaging using an excitation wavelength of 675 nm can be attributed to an aggregation-induced effect, which has been observed in other fluorescent molecules and particles.[53,54]

***In Vitro* Biodegradation.** As mentioned previously, one of the major barriers that must be overcome when using nanoparticles for diagnostic imaging is the issue of liver accumulation. We reasoned that the nanoparticles we have prepared can by biodegraded by biliverdin reductase, which is found in many organs[37,42] but has the highest expression in the liver. When degradation experiments were conducted using biliverdin reductase, we were able to establish the biodegradation profile of these nanoparticles. Degradation experiments were carried out on water-BVNPs and NaCl-BVNPs over a period of seven days, with biotransformation being tracked by UV-Vis spectroscopy and matrix-assisted laser desorption/ionization (MALDI) mass spectrometry. The magnitude of UV-Vis absorbance at 670 nm was used as an indicator for degradation as reported previously.[39] When exposed to biliverdin reductase and its cofactor, nicotinamide adenine dinucleotide hydride (NADH), the absorbance at 670 nm decreased steadily as a function of time (Figure 6A, Figure S8). After seven days of degradation of the 10-min and 24-h water-BVNPs, their absorbances had decreased to 8% and 17% of their initial absorbances respectively. Similarly, the NaCl-BVNP 10-min and 24-h absorbances fell to 9% and 13% of their initial values respectively. A visible color change from a blue-green color for the BVNPs to a yellow color for all degraded nanoparticles was also observed (Figure 6B).

MALDI/TOF spectrometry of water-BVNPs showed peaks at a mass to charge (m/z) value of 583 for the 10-min and 24-h nanoparticles, corresponding to the presence of biliverdin (Figure 6C). These peaks were no longer present after five days of nanoparticle degradation, further

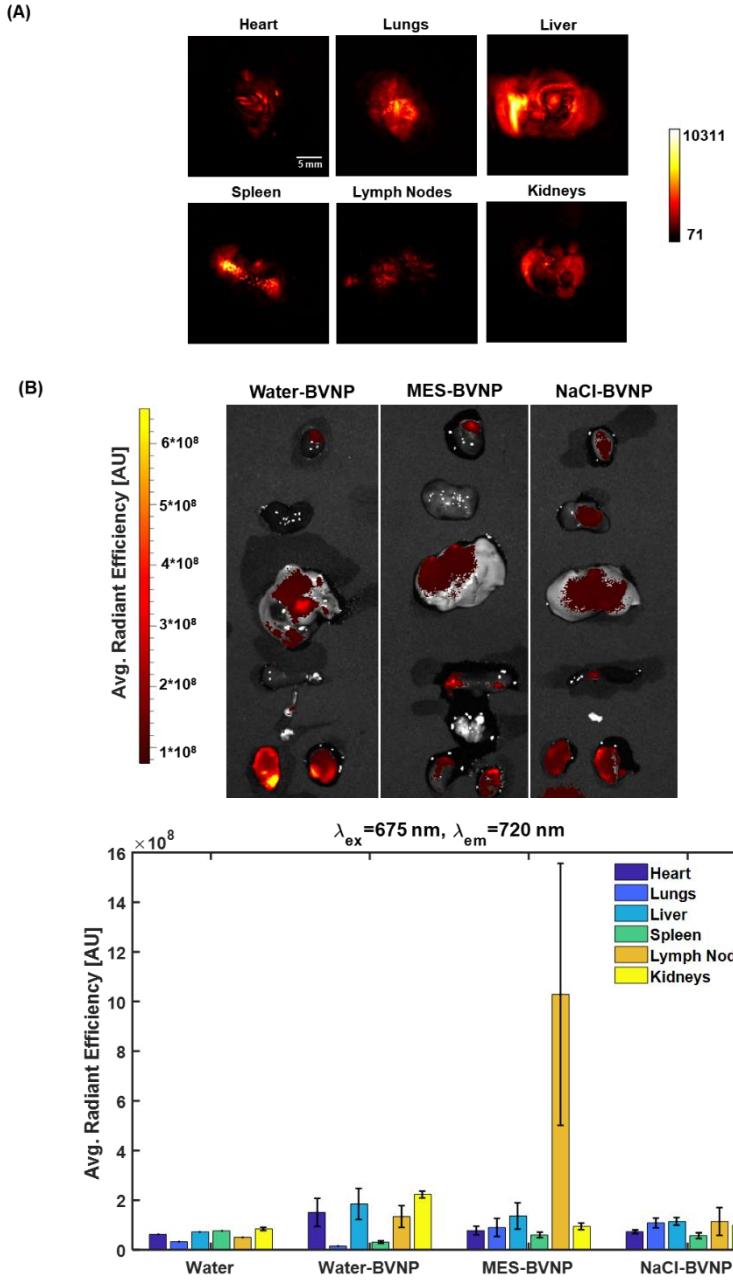

Figure 5. BVNP organ distribution. **(A)** Representative Photoacoustic images of dissected organs from mice treated with NaCl-BVNPs. Generally, similar accumulation was observed in the organs of mice treated with water-BVNPs MES-BVNPs, and NaCl-BVNPs. Here, some nanoparticle accumulation is seen in all organs, with very high nanoparticle accumulation in the liver. **(B)** IVIS fluorescence imaging of dissected organs from mice treated with Water-BVNPs, MES-BVNPs,

and NaCl-BVNPs. The majority of accumulation in BVNP-treated animals was observed in the liver, kidneys, and lungs, with only minor accumulation in the spleen and most lymph nodes. Top to bottom: heart, lungs, liver, spleen, lymph nodes, and kidneys. Aggregation-induced fluorescence shifting resulted in a fluorescence response from BVNPs in organs for an excitation wavelength of 675 nm. Error bars represent standard error across all animals for each nanoparticle type. confirming the breakdown of the nanoparticles as a result of enzymatic degradation. Additionally, peaks at m/z values of 713 and 1277 were present in both the 10-min and 24-h nanoparticles (Figure 6C, Figure S9-10), indicating the covalent linkage of a biliverdin molecule with a single diamine, and the linkage of two biliverdin molecules with a single diamine, respectively. These peaks were found to disappear after five days of degradation. The results indicated biotransformation of BVNPs to bilirubin *via* biliverdin reductase, followed by further degradation by oxidation to produce compounds A, B, C, and D (Figure 6D), which correspond to m/z values of 178, 137, 177, and 135, as confirmed by Electrospray ionization (ESI) mass spectroscopy. The products corresponding to m/z values of 177 and 135 are identified as the keto-enol tautomer of compounds A and B. After five days of degradation of 10-min nanoparticles, several new mass peaks at m/z values of 428 to 1950 were identified, indicative of A, B, C, and D. The products corresponding to m/z values of 550, 666 and 805 were observed over the course of five days degradation of 24-h nanoparticles, indicating the formation of A, B, C, and D. Degradation by the same mechanism was also confirmed *via* mass spectrometry for NaCl-BVNPs (Figures S11-S13).

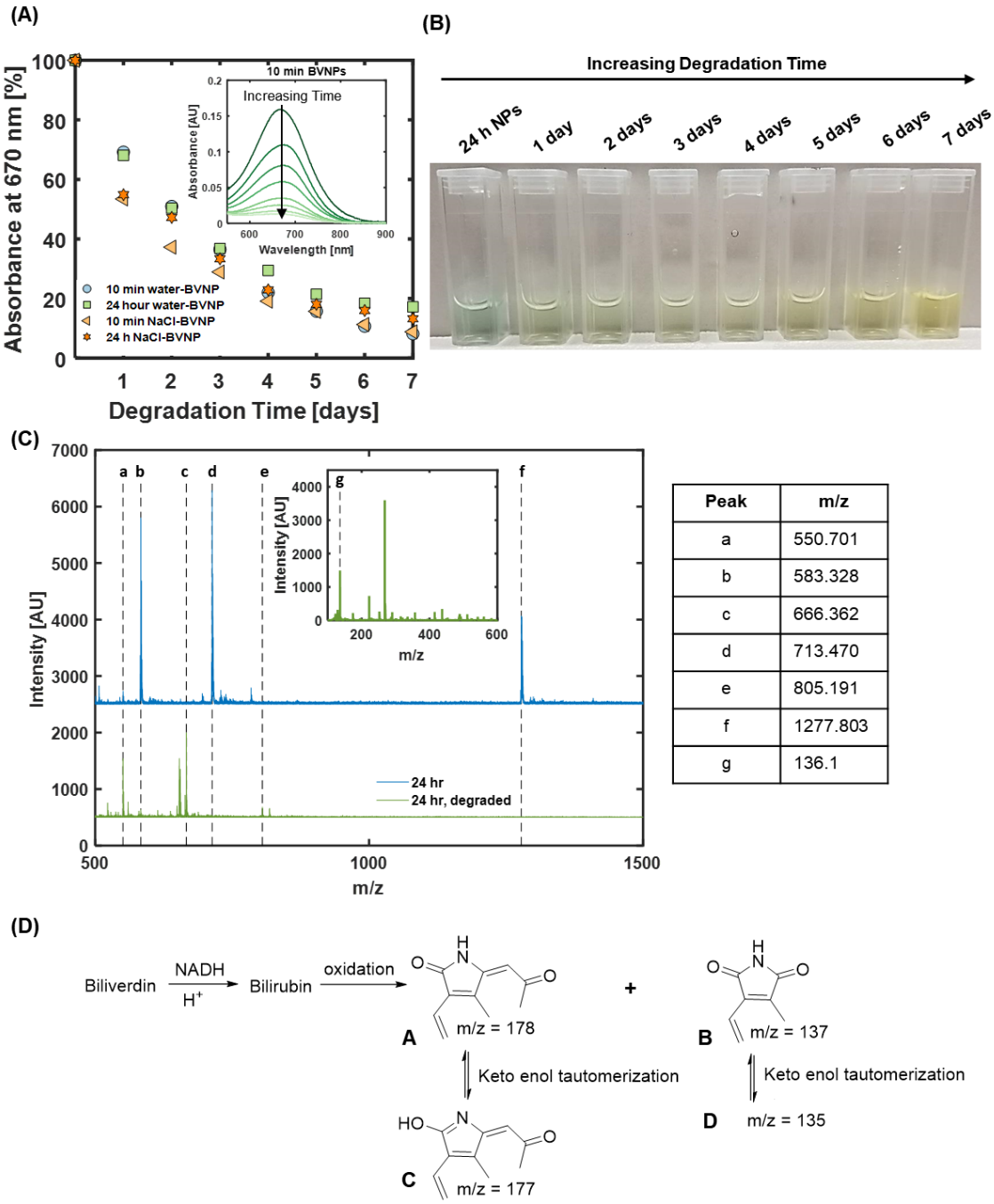

Peak	m/z
a	550.701
b	583.328
c	666.362
d	713.470
e	805.191
f	1277.803
g	136.1

Figure 6. Degradation of water-BVNPs and NaCl-BVNPs. **(A)** UV-Vis absorbance at 670 nm for degraded BVNPs as a percentage of UV-Vis absorbance at 670 nm for BVNPs prior to degradation. Inset depicts 550 nm to 900 nm UV-Vis spectra collected for 10-min water-BVNPs. **(B)** Color change in diluted 24-h BVNPs as a result of increasing degradation time. A shift from blue-green to yellow is observed with an increase in degradation time. **(C)** Mass Spectrometry results for 24-h water-BVNPs. **(D)** Proposed BVNP degradation process.

Degradation experiments carried out on MES-BVNPs in the presence of biliverdin reductase and nicotinamide adenine dinucleotide phosphate (NADPH) (Figure 7A) showed that the MES-BVNPs degrade at a slower rate than that of water-BVNPs and NaCl-BVNPs (Figure 7B), with 10-min and 24-h MES-BVNPs reaching 60.3 and 53.1% of initial MES-BVNP absorbance after 13 days of degradation. This slower degradation is likely due to both a higher BVNP crosslinking efficiency when synthesized in MES, and a change in the enzyme activity due to the lower pH of MES compared to the pH of water and the NaCl solution. The degradation

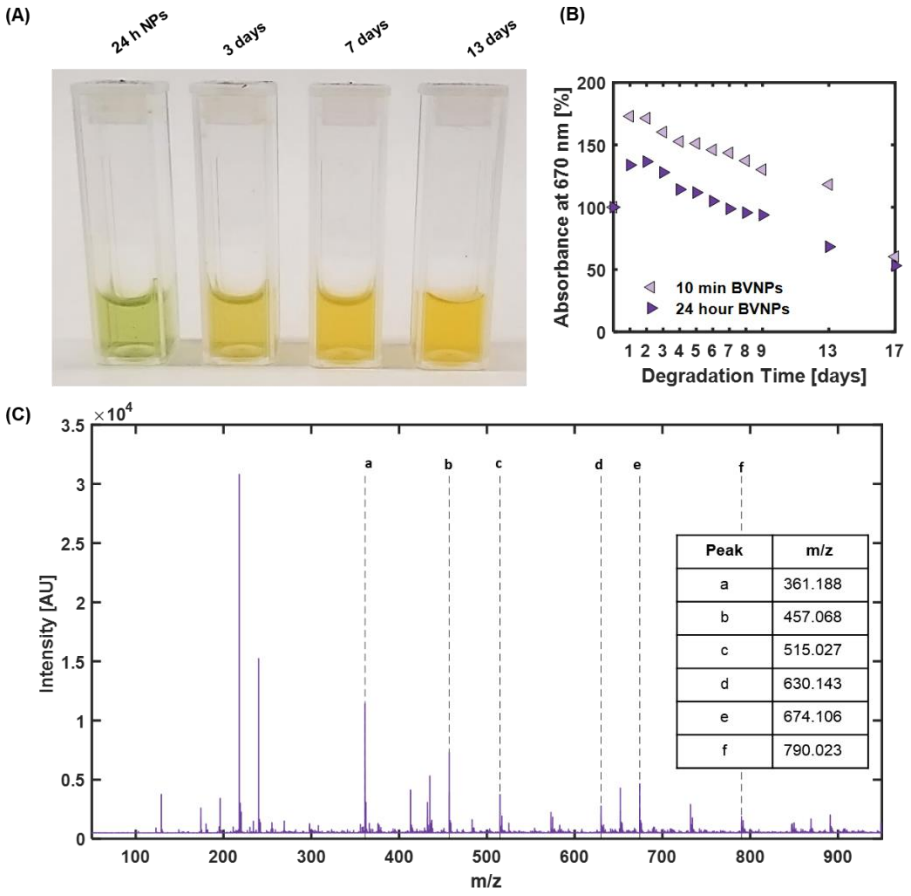

Figure 7. Degradation of MES-BVNPs. **(A)** Color change in diluted 24 h MES-BVNPs as a result of increasing degradation time. A shift from green to yellow is observed with an increase in degradation time. **(B)** UV-Vis absorbance at 670 nm for degraded MES-BVNPs (13 days degradation) as a percentage of UV-Vis absorbance at 670 nm for MES-BVNPs prior to degradation. **(C)** Mass Spectrometry results for degraded 24 h MES-BVNPs.

mechanism for MES-BVNPs was confirmed to be the same as that of water-BVNPs and NaCl-BVNPs *via* mass spectrometry (Figure 7C, Figures S14-S16). Calculations for all spectra are provided in the supplementary information. These results are especially promising because biliverdin reductase occurs naturally in the liver and other organs, pointing towards facile biometabolism of BVNPs.

***In Vivo* Biodegradation.** *In vivo* biodegradation experiments were conducted in order to confirm that the favorable *in vitro* degradation results could be replicated in living organisms. Mice were each administered with water-BVNPs, MES-BVNPs, or NaCl-BVNPs *via* a flank injection. Flank injections were utilized instead of hock injections because the lymphatic system is constantly draining, so any signal decrease with time in the lymph nodes could be attributed to clearance of the nanoparticles by flow through the lymph nodes, rather than degradation of the particles themselves. The flank injections allowed for high accumulation of the nanoparticles in one location rather than their dispersal with flow. This allowed us to study the degradation of the nanoparticles with time. Photoacoustic images of the mice were taken prior to injection, and at 5 min, 24 h, and 96 h after injection for wavelengths of 680 nm (Figure 8A), 720 nm (Figure S17 A), and 750 nm (Figure S17 B). The differences in PA intensity across multiple wavelengths for each particle type can be explained by the nonlinear relationship between absorbance and PA intensity. ROI analysis was conducted in ImageJ to quantify the signal increase after nanoparticle injection, and decrease as a result of degradation (Figure 8B). PA signal increased by at least three-fold upon injection of BVNPs, and then returned to values close to the initial value within 24 h, indicating that the BVNPs had almost completely degraded within 24 h. This was also apparent visually, as the flanks injected with water-BVNPs and NaCl-BVNPs exhibited a visible green color after administration, and this green color was no longer apparent 24 h post-injection. MES-BVNPs

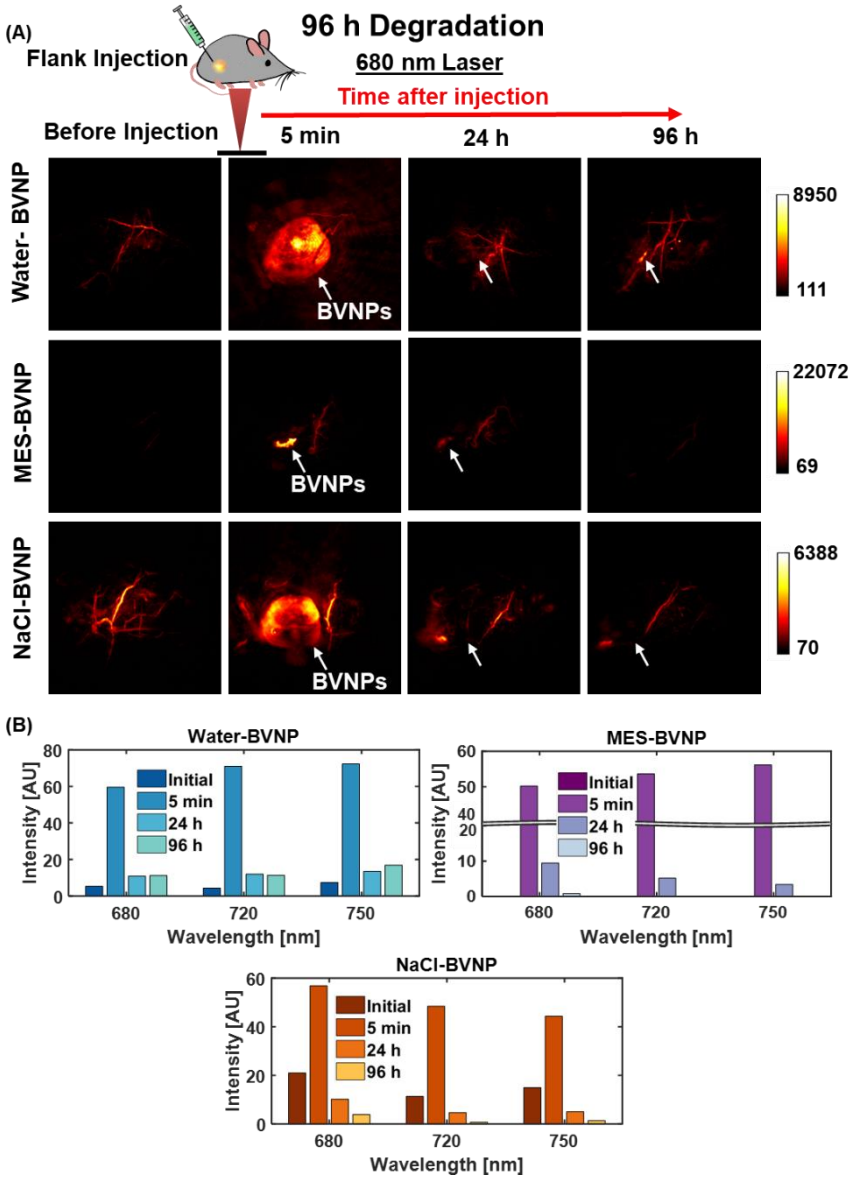

Figure 8. *In vivo* BVNP Degradation over a period of 96 h. **(A)** Photoacoustic images take prior to nanoparticle injection in mouse flanks, and 5 min, 24 h, and 96 h after injection. An increase in signal as a result of BVNP injection, and decrease in signal as a result of BVNP degradation, is observed. Arrows indicate locations of signal increase and decrease as a result of BVNP injection and degradation **(B)** ROI analysis of *in vivo* degradation for each type of BVNP for photoacoustic imaging acquisition wavelengths of 680 nm, 720 nm, and 750 nm. A sharp decrease in signal 24 h post-injection indicates quick *in vivo* degradation.

did not appear as widely distributed immediately after injection as the water-BVNPs and NaCl-BVNPs did, which is likely a result of the properties of the MES solvent. Despite the initially high accumulation of MES-BVNPs at the injection site, the MES-BVNPs also show a favorable *in vivo* degradation profile.

We further sought to explore the degradation behavior of these nanoparticles during the first 24 h after injection. Degradation experiments were repeated with multiple time-points (2 min, 1 h, 6 h, 12 h, 24 h) from initial injection through 24 h after injection. Images were collected at 680 nm (Figure 9A), 720 nm (Figure S16 A), and 750 nm (Figure S18 B). The BVNP signals were found to steadily decrease with time based on ROI analysis (Figure 9B). Taking the initial signal 2 min post-injection to be 100 %, after 24 hours Water-BVNPs, MES-BVNPs, and NaCl-BVNPs had degraded to 44, 23, and 27 % of their initial values respectively. These results indicate that BVNPs are entirely biometabolizable *in vivo*.

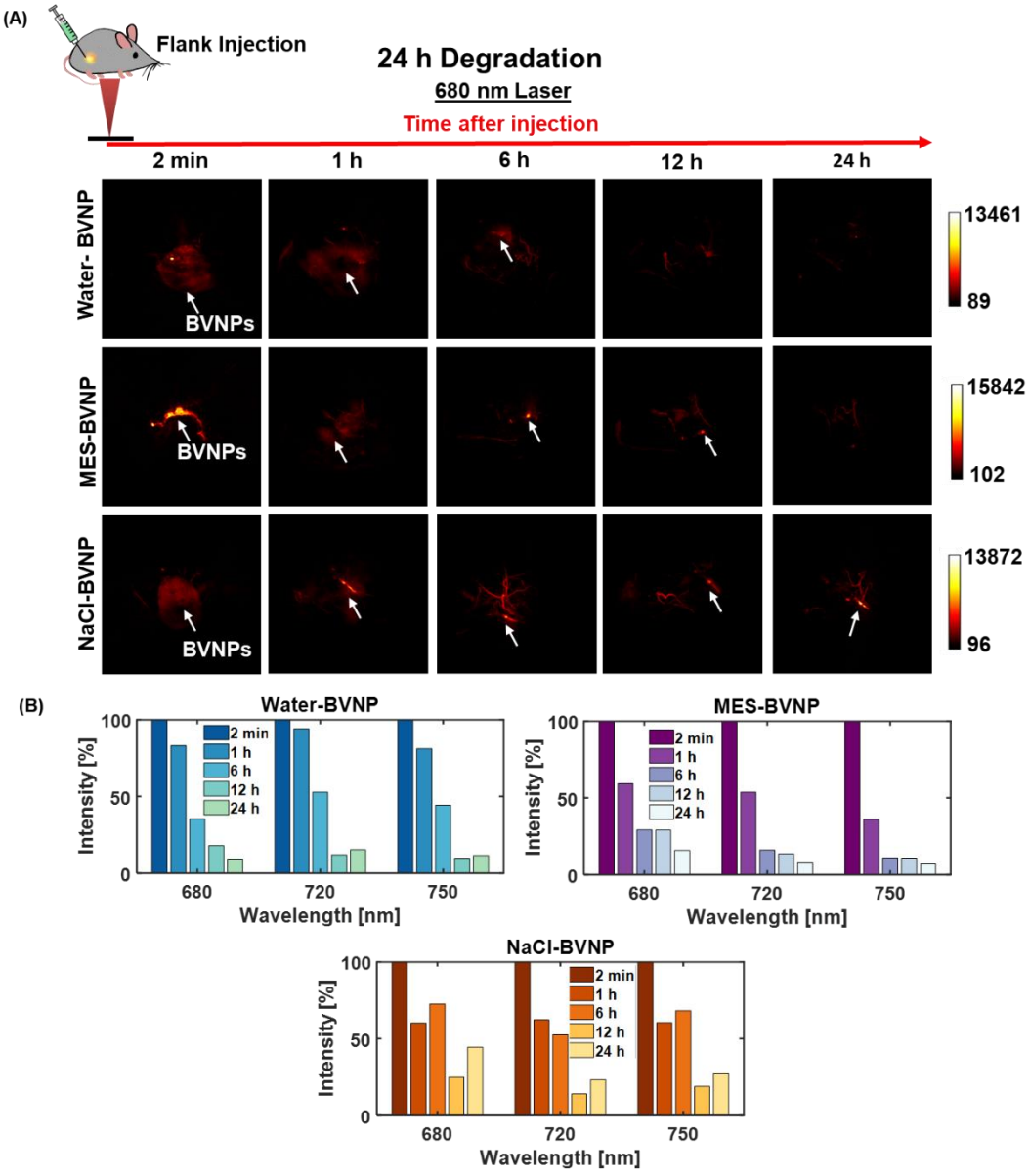

Figure 9. *In vivo* BVNP Degradation over a period of 24 h. **(A)** Photoacoustic images take 2 min, 1 h, 6 h, 12 h, and 24 h after injection in mouse flanks. A decrease in signal as a result of BVNP degradation is observed. Arrows indicate locations of signal increase and decrease as a result of BVNP injection and degradation **(B)** ROI analysis of *in vivo* degradation for each type of BVNP for photoacoustic imaging acquisition wavelengths of 680 nm, 720 nm, and 750 nm. A steady decrease in BVNP signal is observed over a period of 24 h, indicating BVNP degradation with time.

CONCLUSIONS.

Overall, we show that nanoprecipitation of endogenous molecules can lead to spectral tuning based on the choice of reaction media. Due to the inherent water solubility of biliverdin, a simple synthetic process has been developed to synthesize a nano-platform that is fully biodegradable. Water-BVNPs and NaCl-BVNPs displayed high absorbance and low fluorescence in the UV region, while MES-BVNPs had low absorbance and high fluorescence in the UV region, in addition to a fluorescence red-shifting as a function of synthesis time. MES-BVNPs were found to have a higher fluorescence intensity and radiant efficiency than other nanoparticle types, and were also found to have comparable photoacoustic intensity to ICG. Water-BVNP and NaCl-BVNP PA intensity increased with synthesis time, while MES-BVNP PA intensity was unaffected. Biocompatibility of BVNPs was demonstrated through blood smear experiments in addition to MTT assays in MCF-7 and MDA-MB-231 cells.

Injection of BVNPs was found to lead to an increased photoacoustic signal *in vivo* in mice, with some non-specific accumulation in the lymph nodes as expected based on the use of hock injections. The nanoparticles were also found to be biodegradable, degrading in the presence of biliverdin reductase and NADH or NADPH. The complete biodegradation of BVNPs was also demonstrated *in vivo*. BVNPs provide a promising platform for biological imaging due to their inherent photoacoustic and fluorescent properties, as well as their biodegradability. The safety and efficacy of nanomedicines is typically influenced by multiple parameters to create a major bottleneck for translating these agents. The complexity of nanomedicine presented by the multi-component three dimensional constructs demands vigilant design and engineering to achieve the intended physicochemical characteristics and biological behaviors. Designing a system that

‘disappears’ completely from the biological system could offer a potential strategy to accelerate the translation of these agents and accelerate the growth of this critical field.

METHODS.

Materials. Biliverdin hydrochloride was purchased from Sigma-Aldrich and Frontier Scientific. EDC and Sodium Chloride were purchased from Fisher Scientific. N-hydroxysuccinimide (NHS), 2,2’ ethylenedioxy bis(ethylamine), Biliverdin Reductase A human, NADPH tetrasodium salt, and NADH disodium salt were purchased from Sigma Aldrich. MES buffer was purchased from Thermo Scientific.

Synthesis. Biliverdin was dissolved overnight at a concentration of 1 mg/mL using 10 mL of the chosen solvent (filtered water, 0.1 M MES buffer, or 0.9% NaCl solution) in a 20 mL scintillation vial on a stir plate at 500 rpm. The carboxylic acid group on the Biliverdin was then activated using 6.7 mg EDC and 4 mg NHS for 10 min, after which 3.5 µL of the diamine was added to commence the cross-linking reaction. The resulting nanoparticles are referred to as water-BVNPs, MES-BVNPs, and NaCl-BVNPs depending on the respective solvent used for nanoparticle synthesis. Samples were collected at 10 min, 6 h, 12 h, and 24 h. Unless otherwise noted, in experiments for which dialyzed BVNPs were used, BVNPs were dialyzed against 500 mL of their respective synthesis solvents using dialysis cassettes with a cutoff of 10 kDa, and sample size of 3 mL.

Microscopy. TEM samples were prepared immediately *via* drop-casting of 2.5 µL diluted nanoparticle solution (10 µL of the nanoparticle solution diluted with 90 µL filtered water) on copper TEM grids. Excess moisture was wicked away after 2 minutes. TEM images were taken

on a JEOL Cryo 2100 TEM using an acceleration voltage of 20 keV. Nanoparticle size was determined using ImageJ.

Spectroscopy. UV-Vis measurements were performed on samples using a Thermo Scientific Genesys 10S UV-Vis Spectrophotometer immediately after sample collection and dilution. For these measurements, 10 µL of the nanoparticle solution was diluted with 990 µL of the synthesis solvent, and the baseline measurement was taken using the synthesis solvent for each nanoparticle type. The UV-Vis spectra were collected over the 225 nm to 800 nm range.

Fluorescence measurements were taken using a TECAN infinite M200 PRO fluorescence spectrometer at excitation wavelengths of 365 nm and 680 nm, with a measured emission range of 365-850 nm and 680-680 nm respectively. Images were also taken of undiluted 24 h time point BVNPs under a 365 nm wavelength UV lamp. Zeta potential measurements were taken for the 10-min and 24-h time points using a Malvern Zetasizer.

FT-IR samples were prepared by dropping 500 µL of the nanoparticle solution onto Kevley MirrIR Corner Frosted FT-IR slides and allowing sit overnight, after which they were placed under vacuum until they had completely dried. FT-IR measurements were taken using a Thermo Nicolet Nexus 670 FT-IR.

Hydrodynamic Size, particle concentration, and calculations. Nanoparticle hydrodynamic size, size distribution, and concentration were measured using a Malvern Panalytical NanoSight NS300. Dialyzed nanoparticles were utilized for these experiments. 10 1-minute videos were recorded for each nanoparticle type, with average hydrodynamic size, mode hydrodynamic size, size distributions, and concentrations calculated for each nanoparticle type. 10 µL of Water-BVNPs and MES-BVNPs were diluted in 990 µL of their respective synthesis solvents for these

measurements. For NaCl-BVNPs, 100 µL of the particles were diluted in 900 µL NaCl solution. These dilution factors were taken into consideration for calculation of the final concentrations. Taking into consideration the remaining mass of biliverdin in each type of particle (as determined by UV-Vis spectroscopy), the average mass of each nanoparticle type and the average number of biliverdin molecules were then calculated using the following equations:

$$Average\ Particle\ Mass\ [mg] = \frac{Incorporated\ biliverdin\ \left[\frac{mg}{mL}\right]}{Particle\ concentration\ [mL^{-1}]} \quad (1)$$

$$Number\ of\ biliverdin\ molecules\ per\ particle = \frac{Average\ Particle\ Mass\ [mg]}{BIliverdin\ molecular\ weight\ \left[\frac{mg}{mol}\right]} * 6.022 * 10^{23}\left[\frac{molecules}{mol}\right] \quad (2)$$

Photoacoustic Imaging. Photoacoustic imaging was conducted using an Endra Nexus 128 photoacoustic tomographer with excitation wavelengths of 680 nm, 720 nm, 750 nm, and 800 nm (continuous rotation mode, 6 second rotation time).

Tissue-mimicking Phantom Preparation. Agarose (2 g) was dissolved in a solution containing deionized water (39 mL) and 2% milk (1 mL). The solution was heated in a microwave oven for 30 seconds, removed and stirred, and then heated for an additional 15 sections to produce a viscous gel. The mixture was then poured into a custom Teflon mold designed with the same specifications as the Endra Nexus 128 PA tomographer bowl (Figure S3). For *in vitro* phantom studies, hypodermic steel tubing was inserted into the Teflon mold as a placeholder for fluorinated ethylene propylene tubing used to contain the samples.

Comparison with ICG. Tissue phantom imaging was conducted on 24-h water-BVNPs, MES-BVNPs, and NaCl-BVNPs which were dialyzed with their respective synthesis solvents. ICG at

the same final mass concentrations was used for comparison. The final mass concentration of biliverdin in each type of BVNP was determined by taking the ratio of 365 nm absorbance after dialysis to before dialysis. Two 200 μL samples were used in each tissue phantom experiment, with a total of 3 technical replicates for each type of particle.

Comparison of 10 min and 24 h BVNPs. Tissue phantom imaging was conducted as before, but with 200-μL 10 min water-BVNPs, 24 h water-BVNPs, 10 min MES-BVNPs, 24 h MES-BVNPs, 10 min NaCl-BVNPs, and 24 h NaCl-BVNPs, each of which were dialyzed with their respective synthesis solvents. In addition, imaging was conducted on 24 h MES-BVNPs which were dialyzed with water. Three technical replicates were used for each sample. ROI analysis in ImageJ was used to determine the average PA intensity for each sample.

Blood Smear. Fresh whole pig blood was collected from the UIUC Meat Laboratory in citrate-coated blood collection tubes. Samples were stored until use, at which time any coagulated blood was removed through centrifugation at 1000 rpm for 1 minute. 180 μL of uncoagulated blood was placed in each of 7 0.7-mL centrifuge tubes. For experimental samples, 20 μL of BVNP solution (10 min water-BVNPs, 24 h water-BVNPs, 10 min MES-BVNPs, 24 h MES-BVNPs, 10 min NaCl-BVNPs, or 24 h NaCl-BVNPs) was added to the blood sample. All particles used were dialyzed with their respective synthesis solvents. The blood-nanoparticle solution was gently mixed through repeated pipetting, after which samples were incubated at room temperature for 30 min. Following this incubation period, 50 μL of each sample was deposited on individual glass slides, and a second clean glass slide was used to spread these samples uniformly across the slides. Optical microscopy was conducted immediately after slide preparation.

Cell Viability. MTT assays were separately conducted on MCF-7 cells and MDA-MB-231 cells exposed to 5 % by volume, and 10 % by volume of 10 min and 24 h water-BVNPs, MES-BVNPs, and NaCl-BVNPs dialyzed with their respective synthesis solvents. Cells were cultured in T-25 flasks using DMEM completed with 10 % fetal bovine serum (FBS) and 1 % penicillin-streptomycin. Cells were plated in 96-well plates at a density of 10,000 cells/well, with 100 µL of cells added to each well. Cells were allowed to grow for 24 h, after which media was removed and replaced with 100 µL fresh media containing 5 % by volume or 10 % by volume BVNP solution. 4 wells were used for each experimental sample, and 12 wells were used for the control (untreated) samples. Cells were incubated with these solutions for 24 h at 37 °C, after which media was removed and cells were rinsed with DPBS. 100 µL fresh media was then added to each well, followed by 15 µL MTT (MCF-7 cells) or 10 µL MTT (MDA-MB-231 cells). Cells were then incubated at 37 °C for 4 h. The media-MTT solution was then removed and 100 µL DMSO was added to each well to dissolve the formazan crystals. Viability was assessed by measuring the absorbance of each well at 570 nm and 630 nm on a Biotek Cytation 5 plate reader. Cell viability as a percentage of control cell viability was determined using the following equation:

$$\%\, Viability = \left(\frac{Sample\ Abs_{570} - Sample\ Abs_{630}}{Control\ Abs_{570} - Control\ Abs_{630}}\right) * \ 100\% \tag{3}$$

Fluorescence Imaging. Fluorescence imaging was conducted using an IVIS imaging system. Excitation wavelengths ranging from 430 nm to 710 nm were used, and as-prepared 10-min and 24-h water-BVNPs, MES-BVNPs, and NaCl-BVNPs were imaged.

***In Vivo* Studies.** To evaluate the *in vivo* imaging ability of the BVNPs in different solvent systems, animal experiments were performed with the minimum required number of animals. The

experimental protocol was approved by the Institutional Animal Care and Use Committee (IACUC), University of Illinois, Urbana−Champaign, and satisfied all University and National Institutes of Health (NIH) rules for the humane use of laboratory animals. Athymic mice were bought from Charles River Laboratories International, Inc. U.S.A. Upon arrival, athymic mice were allowed one week for acclimation. Animals were single-cage housed and had free access to food and water. Animals were housed in Beckman Institute, University of Illinois at Urbana-Champaign.

Lymph Node Imaging. A total of three groups of nude mice were used for *in vivo* demonstration of photoacoustic imaging, and one animal was used as the control. Animals in group one were treated with Water-BVNPs (n=3), animals in group two were treated with MES-BVNPs (n=3), and animals in group three were treated with NaCl-BVNPs (n=3). All nanoparticles were used post-dialysis of the 24-h timepoint. The mice were injected *via* a hock injection with 50 μL of the respective BVNP type in their rear leg. The control mouse was injected with water alone. Photoacoustic images were taken prior to injection, and 5 min, 10 min, 15 min, and 30 min post-injection. Images were acquired for wavelengths of 680 nm, 720 nm, and 750 nm. Mice were sacrificed after image acquisition at 30 minutes, and their organs were subsequently dissected. Photoacoustic images were taken of the dissected organs (heart, lungs, liver, spleen, lymph nodes, and kidneys). Fluorescence imaging of these organs was also conducted with an excitation wavelength of 675 nm.

In Vivo Degradation. Three mice were used for *in vivo* demonstration of biodegradation, one for each BVNP type. All nanoparticles were used post-dialysis of the 24-h timepoint. 50 μL of nanoparticle solution was injected subcutaneously in the flank of each mouse. Images were taken

prior to injection, 5 min, 24 h, and 96 h after injection. In further experiments, images were taken 2 min, 1 h, 6 h, 12 h, and 24 h after injection. ROI analysis was conducted in ImageJ.

Water-BVNP and NaCl-BVNP Degradation Experiments. Degradation experiments were conducted on 1 mL each of 10-min and 24-h as-prepared water-BVNPs and NaCl-BVNPs. The nanoparticles were placed in 4 mL glass vials on a stirplate at 500 rpm with a temperature of 40 ˚C. 40 mg of NADH was then added to each vial, and allowed to dissolve for 10 min. 2 μL of the Biliverdin Reductase were then added to each vial, beginning the degradation experiment. 12 μL samples were taken from each vial every 24 h. Of these 12 μL, 10 μL was diluted with 990 μL of water in one UV-Vis cuvette, and the remaining 2 μL was diluted with 998 μL of water in another UV-Vis cuvette. UV-Vis measurements were taken in the range of 300 to 900 nm for the 2:998 μL dilution, and in the range of 550 to 900 nm for the 10:990 dilution. These ranges and dilutions were chosen because the NADH itself caused an increase in absorbance at 340 nm, which led to an absorbance of greater than one for the regular 10:990 dilution when the spectra were collected in the range of 300 to 900 nm. After UV-Vis measurements were taken, 50 μL of each 10:990 dilution were collected for mass spectrometry. The degradation experiment was conducted for a total of 7 days, with mass spectrometry being conducted for the first and fifth days.

MES-BVNP Degradation Experiments. Degradation experiments were conducted on MES-BVNPs as was conducted for water-BVNPs and NaCl-BVNPs. However, 47 mg NADPH was utilized in place of NADH for each mL of MES-BVNPs to be degraded. 50 μL samples were collected for UV-Vis analysis every 24 h for the first 9 days, and then at 13 and 17 days. UV-Vis spectra were collected between 550 and 900 nm, with a dilution of 50 μL nanoparticles to 950 μL MES buffer. This concentration was selected due to the lower absorbance of MES-BVNPs in this

region compared to the water-BVNPs and NaCl-BVNPs. 30-50 μL samples were collected for mass spectrometry prior to degradation and after 13 days of degradation.

Statistical Analysis. All statistical tests were conducted using Student's T-tests assuming unequal variances.

ASSOCIATED CONTENT

Supporting Information.

The following supporting information files are available online free of charge.
Supplementary information and figures (PDF), including UV-Vis plots from the degradation study, 10 min and 24 h BVNP PA imaging in tissue phantoms, in-vivo PA lymph node and degradation imaging at 720 and 750 nm, in-vitro biocompatibility studies, and further mass spectrometry plots and calculations.

AUTHOR INFORMATION

Corresponding Author

* Dipanjan Pan: dipanjan@illinois.edu.

* Jefferson Chan: jeffchan@illinois.edu.

Author Contributions

The manuscript was written through contributions of all authors. All authors have given approval to the final version of the manuscript.

ACKNOWLEDGMENT

This work was carried out in part in the Frederick Seitz Materials Research Laboratory Central Research Facilities, University of Illinois and the Beckman Institute of Advanced Science and Technology, University of Illinois. We gratefully acknowledge Aaron S. Schwartz-Duval for his assistance with zeta potential measurements, Leilei Yin (Beckman Institute) for his assistance with the Nanosight measurements, and the Chemical and Biomolecular Engineering department shared facilities for access to their fluorescence spectrometer. This project was funded through grants from National Institute of Health, Department of Defense, and University of Illinois. P. Fathi was supported by the National Physical Science Consortium and the National Institute of Standards & Technology through an NPSC graduate fellowship and by the Nadine Barrie Smith Memorial Fellowship from the Beckman Institute. H. Knox was supported by a graduate fellowship from the Beckman Institute. Research reported in this publication was supported by the National Institute of Biomedical Imaging and Bioengineering of the National Institutes of Health under Award Number T32EB019944. Any mention of commercial products is for information only; it does not imply recommendation or endorsement by NIST.

REFERENCES

(1) Knox, H. J.; Chan, J. Acoustogenic Probes: A New Frontier in Photoacoustic Imaging. *Acc. Chem. Res.* **2018**, *51*, 2897–2905.

(2) Zhang, Y.; Wang, L.; Liu, L.; Lin, L.; Liu, F.; Xie, Z.; Tian, H.; Chen, X. Engineering Metal Organic Frameworks for Photoacoustic Imaging Guided Chemo/Photothermal Combinational Tumor Therapy. *ACS Appl. Mater. Interfaces* **2018**, *10*, 41035−41045.

(3) Qiao, Y.; Gumin, J.; Maclellan, C. J.; Gao, F.; Bouchard, R.; Lang, F. F.; Stafford, R. J.; Melancon, M. P. Magnetic Resonance and Photoacoustic Imaging of Brain Tumor Mediated by Mesenchymal Stem Cell Labeled with Multifunctional Nanoparticle Introduced via Carotid Artery Injection. *Nanotechnology* **2018**, *29*, 1–11.

(4) Kwon, H. J.; Shin, K.; Soh, M.; Chang, H.; Kim, J.; Lee, J.; Ko, G.; Kim, B. H.; Kim, D.; Hyeon, T. Large-Scale Synthesis and Medical Applications of Uniform-Sized Metal Oxide Nanoparticles. *Adv. Mater.* **2018**, *30*, 1–24.

(5) Köker, T.; Tang, N.; Tian, C.; Zhang, W.; Wang, X.; Martel, R.; Pinaud, F. Cellular Imaging by Targeted Assembly of Hot-Spot SERS and Photoacoustic Nanoprobes Using Split-Fluorescent Protein Scaffolds. *Nat. Commun.* **2018**, *9*, 607.

(6) Kim, T.; Zhang, Q.; Li, J.; Zhang, L.; Jokerst, J. V. A Gold/Silver Hybrid Nanoparticle for Treatment and Photoacoustic Imaging of Bacterial Infection. *ACS Nano* **2018**, *12*, 5615–5625.

(7) Kang, J.; Kim, D.; Wang, J.; Han, Y.; Zuidema, J. M.; Hariri, A.; Park, J. H.; Jokerst, J. V.; Sailor, M. J. Enhanced Performance of a Molecular Photoacoustic Imaging Agent by Encapsulation in Mesoporous Silicon Nanoparticles. *Adv. Mater.* **2018**, *30*, 1–8.

(8) Huang, Y.; Li, F.; Ma, G.; Yang, W.; Zhang, X.; Lin, J.; Luo, Y.; Huang, P. Aggregation Induced Photoacoustic Detection of Mercury (Ⅱ) Ions Using Quaternary Ammonium Group-Capped Gold Nanorods. *Talanta* **2018**, *187*, 65–72.

(9) Hanske, C.; Sanz-Ortiz, M. N.; Liz-Marzán, L. M. Silica-Coated Plasmonic Metal Nanoparticles in Action. *Adv. Mater.* **2018**, *30*, 1–28.

(10) Hajfathalian, M.; Amirshaghaghi, A.; Naha, P. C.; Chhour, P.; Hsu, J. C.; Douglas, K.; Dong, Y.; Sehgal, C. M.; Tsourkas, A.; Neretina, S.; Cormode, D. P. Wulff in a Cage Gold Nanoparticles as Contrast Agents for Computed Tomography and Photoacoustic Imaging. *Nanoscale* **2018**, *10*, 18749–18757.

(11) Tang, W.; Yang, Z.; Wang, S.; Wang, Z.; Song, J.; Yu, G.; Fan, W.; Dai, Y.; Wang, J.; Shan, L.; Niu, G.; Fan, Q.; Chen, X. Organic Semiconducting Photoacoustic Nanodroplets for Laser-Activatable Ultrasound Imaging and Combinational Cancer Therapy. *ACS Nano* **2018**, *12*, 2610–2622.

(12) Yin, C.; Wen, G.; Liu, C.; Yang, B.; Lin, S.; Huang, J.; Zhao, P.; Wong, S. H. D.; Zhang,

K.; Chen, X.; Li, G.; Jiang, X.; Huang, J.; Pu, K.; Wang, L.; Bian, L. Organic Semiconducting Polymer Nanoparticles for Photoacoustic Labelling and Tracking of Stem Cells in the Second Near-Infrared Window. *ACS Nano* **2018**, *12*, 12201–12211.

(13) Guo, B.; Sheng, Z.; Hu, D.; Liu, C.; Zheng, H.; Liu, B. Through Scalp and Skull NIR-II Photothermal Therapy of Deep Orthotopic Brain Tumors with Precise Photoacoustic Imaging Guidance. *Adv. Mater.* **2018**, *30*, 1–8.

(14) Qin, X.; Chen, H.; Yang, H.; Wu, H.; Zhao, X.; Wang, H.; Chour, T.; Neofytou, E.; Ding, D.; Daldrup-Link, H.; Heilshorn, S. C.; Li, K.; Wu, J. C. Photoacoustic Imaging of Embryonic Stem Cell-Derived Cardiomyocytes in Living Hearts with Ultrasensitive Semiconducting Polymer Nanoparticles. *Adv. Funct. Mater.* **2018**, *28*, 1–12.

(15) Jung, E.; Kang, C.; Lee, J.; Yoo, D.; Hwang, D. W.; Kim, D.; Park, S. C.; Lim, S. K.; Song, C.; Lee, D. Molecularly Engineered Theranostic Nanoparticles for Thrombosed Vessels: H2O2-Activatable Contrast-Enhanced Photoacoustic Imaging and Antithrombotic Therapy. *ACS Nano* **2018**, *12*, 392–401.

(16) Pan, D.; Pramanik, M.; Senpan, A.; Ghosh, S.; Wickline, S. a.; Wang, L. V.; Lanza, G. M. Near Infrared Photoacoustic Detection of Sentinel Lymph Nodes with Gold Nanobeacons. *Biomaterials* **2010**, *31*, 4088–4093.

(17) Pan, D.; Cai, X.; Yalaz, C.; Senpan, A.; Omanakuttan, K.; Wickline, S. a.; Wang, L. V.; Lanza, G. M. Photoacoustic Sentinel Lymph Node Imaging with Self-Assembled Copper Neodecanoate Nanoparticles. *ACS Nano* **2012**, *6*, 1260–1267.

(18) Pan, D.; Cai, X.; Kim, B.; Stacy, A. J.; Wang, L. V.; Lanza, G. M. Rapid Synthesis of near Infrared Polymeric Micelles for Real-Time Sentinel Lymph Node Imaging. *Adv. Healthc. Mater.* **2012**, *1*, 582–589.

(19) Song, K. H.; Kim, C.; Cobley, C. M.; Xia, Y.; Wang, L. V. Noninvasive Photoacoustic Sentinel Lymph Node Mapping Using Au Nanocages as a Lymph Node Tracer in a Rat Model. **2009**, *9*, 183–188.

(20) Kobayashi, H.; Kawamoto, S.; Bernardo, M.; Brechbiel, M. W.; Knopp, M. V.; Choyke, P. L. Delivery of Gadolinium-Labeled Nanoparticles to the Sentinel Lymph Node: Comparison of the Sentinel Node Visualization and Estimations of Intra-Nodal Gadolinium Concentration by the Magnetic Resonance Imaging. *J. Control. Release* **2006**, *111*, 343–351.

(21) Akers, W. J.; Kim, C.; Berezin, M.; Guo, K.; Fuhrhop, R.; Lanza, G. M.; Fischer, G. M.; Daltrozzo, E.; Zumbusch, A.; Cai, X.; Wang, L. V; Achilefu, S. Noninvasive Photoacoustic and Fluorescence Sentinel Lymph Node Identification Using Dye-Loaded Perfluorocarbon Nanoparticles. *ACS Nano* **2011**, *5*, 173–182.

(22) Zhang, Y. N.; Poon, W.; Tavares, A. J.; McGilvray, I. D.; Chan, W. C. W. Nanoparticle–Liver Interactions: Cellular Uptake and Hepatobiliary Elimination. *J. Control. Release* **2016**, *240*, 332–348.

(23) Piao, M. J.; Kang, K. A.; Lee, I. K.; Kim, H. S.; Kim, S.; Choi, J. Y.; Choi, J.; Hyun, J. W. Silver Nanoparticles Induce Oxidative Cell Damage in Human Liver Cells through Inhibition of Reduced Glutathione and Induction of Mitochondria-Involved Apoptosis. *Toxicol. Lett.* **2011**, *201*, 92–100.

(24) Sharma, V.; Anderson, D.; Dhawan, A. Zinc Oxide Nanoparticles Induce Oxidative DNA Damage and ROS-Triggered Mitochondria Mediated Apoptosis in Human Liver Cells (HepG2). *Apoptosis* **2012**, *17*, 852–870.

(25) Bhattacharya, R.; Mukherjee, P. Biological Properties of "Naked" Metal Nanoparticles. *Adv. Drug Deliv. Rev.* **2008**, *60*, 1289–1306.

(26) Hussain, S. M.; Hess, K. L.; Gearhart, J. M.; Geiss, K. T.; Schlager, J. J. *In Vitro* Toxicity of Nanoparticles in BRL 3A Rat Liver Cells. *Toxicol. Vitr.* **2005**, *19*, 975–983.

(27) Chen, Y. S.; Hung, Y. C.; Liau, I.; Huang, G. S. Assessment of the *In Vivo* Toxicity of Gold Nanoparticles. *Nanoscale Res. Lett.* **2009**, *4*, 858–864.

(28) Schrand, A. M.; Rahman, M. F.; Hussain, S. M.; Schlager, J. J.; Smith, D. A.; Syed, A. F. Metal-Based Nanoparticles and Their Toxicity Assessment. *Wiley Interdiscip. Rev. Nanomedicine Nanobiotechnology* **2010**, *2*, 544–568.

(29) Jeng, H. A.; Swanson, J. Toxicity of Metal Oxide Nanoparticles in Mammalian Cells. *J. Environ. Sci. Heal. - Part A Toxic/Hazardous Subst. Environ. Eng.* **2006**, *41*, 2699–2711.

(30) Anselmo, A. C.; Mitragotri, S. A Review of Clinical Translation of Inorganic Nanoparticles. *AAPS J.* **2015**, *17*, 1041–1054.

(31) Ehlerding, E. B.; Chen, F.; Cai, W. Biodegradable and Renal Clearable Inorganic Nanoparticles. *Adv. Sci.* **2015**, *3*, 1–8.

(32) Phillips, E.; Penate-Medina, O.; Zanzonico, P. B.; Carvajal, R. D.; Mohan, P.; Ye, Y.; Humm, J.; Gönen, M.; Kalaigian, H.; Schöder, H.; Strauss, H. W.; Larson, S. M.; Wiesner, U.; Bradbury, M. S. Clinical Translation of an Ultrasmall Inorganic Optical-PET Imaging Nanoparticle Probe. *Sci. Transl. Med.* **2014**, *6*, 1–9.

(33) Lin, M. M.; Kim, D. K.; El Haj, A. J.; Dobson, J. Development of Superparamagnetic Iron Oxide Nanoparticles (SPIONS) for Translation to Clinical Applications. *IEEE Trans. Nanobioscience* **2008**, *7*, 298–305.

(34) Liu, G.; Gao, J.; Ai, H.; Chen, X. Applications and Potential Toxicity of Magnetic Iron Oxide Nanoparticles. *Small* **2013**, *9*, 1533–1545.

(35) Choi, H. S.; Frangioni, J. V. Nanoparticles for Biomedical Imaging: Fundamentals of Clinical Translation. *Mol. Imaging* **2010**, *9*, 291–310.

(36) Takeda, T.; Mu, A.; Tai, T. T.; Kitajima, S.; Taketani, S. Continuous de Novo Biosynthesis of Haem and Its Rapid Turnover to Bilirubin Are Necessary for Cytoprotection against Cell

Damage. *Sci. Rep.* **2015**, *5*, 1–12.

(37) Wegiel, B.; Otterbein, L. E. Go Green: The Anti-Inflammatory Effects of Biliverdin Reductase. *Front. Pharmacol.* **2012**, *3*, 1–8.

(38) Öllinger, R.; Yamashita, K.; Bilban, M.; Erat, A.; Kogler, P.; Thomas, M.; Csizmadia, E.; Usheva, A.; Margreiter, R.; Bach, F. H. Bilirubin and Biliverdin Treatment of Atherosclerotic Diseases. *Cell Cycle* **2007**, *6*, 39–43.

(39) Singleton, J. W.; Laster, L. Biliverdin Reductase of Guinea Pig Liver. *J. Biol. Chem.* **1966**, *240*, 5518–5525.

(40) Shu, X.; Royant, A.; Lin, M. Z.; Aguilera, T. a; Lev-ram, V.; Steinbach, A.; Tsien, R. Y. Mammalian Expression of Infrared Fluorescent Proteins Engineered from a Bacterial Phytochrome. *Science.* **2009**, *324*, 804–807.

(41) Lee, D. Y.; Kim, J. Y.; Lee, Y.; Lee, S.; Miao, W.; Kim, H. S.; Min, J. J.; Jon, S. Black Pigment Gallstone-Inspired Platinum-Chelated Bilirubin Nanoparticles for Combined Photoacoustic Imaging and Photothermal Therapy of Cancers. *Angew. Chemie - Int. Ed.* **2017**, *56*, 13684–13688.

(42) Maines, M. D. New Insights into Biliverdin Reductase Functions: Linking Heme Metabolism to Cell Signaling. *Physiology* **2005**, *20*, 382–389.

(43) Keating, C. S.; McClure, B. a.; Rack, J. J.; Rubtsov, I. V. Sulfoxide Stretching Mode as a Structural Reporter *via* Dual-Frequency Two-Dimensional Infrared Spectroscopy. *J. Chem. Phys.* **2010**, *133*, 1–14.

(44) Knox, H. J.; Kim, T. W.; Zhu, Z.; Chan, J. Photophysical Tuning of N-Oxide-Based Probes Enables Ratiometric Photoacoustic Imaging of Tumor Hypoxia. *ACS Chem. Biol.* **2018**, *13*, 1838–1843.

(45) Marshall, M. V; Rasmussen, J. C.; Tan, I.; Aldrich, M. B.; Kristen, E.; Wang, X.; Fife, C. E.; Maus, E. A.; Smith, L. A.; Eva, M. Near-Infrared Fluorescence Imaging in Humans with Indocyanine Green: A Review and Update. *Open Surg Oncol J.* **2012**, *2*, 12–25.

(46) Su, Z.; Ye, P.; Teng, Y.; Zhang, L.; Shu, X. Adverse Reaction in Patients with Drug Allergy History After Simultaneous Intravenous Fundus Fluorescein. *J. Ocul. Pharmacol. Ther.* **2012**, *28*, 410–413.

(47) Hartman, K.; Ma, T.-J.; Levi, J.; Gambhir, S. S.; Kothapalli, S. R.; Khuri-Yakub, B. T. Design, Synthesis, and Imaging of an Activatable Photoacoustic Probe. *J. Am. Chem. Soc.* **2010**, No. 14.

(48) Buschmann, V.; Weston, K. D.; Sauer, M. Spectroscopic Study and Evaluation of Red-Absorbing Fluorescent Dyes. *Bioconjug. Chem.* **2003**, *14*, 195–204.

(49) Boguta, A.; Wróbel, D. Fluorescein and Phenolphthalein - Correlation of Fluorescence and

Photoelectric Properties. *J. Fluoresc.* **2001**, *11*, 129–137.

(50) Kim, J.; Park, S.; Choi, W.; Park, G. B.; Jeong, U.; Kim, C. Contrast-Enhanced Photoacoustic Imaging with an Optical Wavelength of 1064 Nm. *Photons Plus Ultrasound Imaging Sens. 2018* **2018**, *10494*, 1–5.

(51) Koo, J.; Jeon, M.; Oh, Y.; Kang, H. W.; Kim, J.; Kim, C.; Oh, J. *In Vivo* Non-Ionizing Photoacoustic Mapping of Sentinel Lymph Nodes and Bladders with ICG-Enhanced Carbon Nanotubes. *Phys. Med. Biol.* **2012**, *57*, 7853–7862.

(52) Kim, C.; Song, K. H.; Gao, F.; Wang, L. V. Sentinel Lymph Nodes and Lymphatic Vessels : Noninvasive Dual-Modality *In Vivo* Mapping by Using Indocyanine Green in Rats — Volumetric Spectroscopic Photoacoustic Imaging and Planar Fluorescence Imaging. *Radiology* **2010**, *255*, 442–450.

(53) Zhang, X.; Zhang, X.; Tao, L.; Chi, Z.; Xu, J.; Wei, Y. Aggregation Induced Emission-Based Fluorescent Nanoparticles: Fabrication Methodologies and Biomedical Applications. *J. Mater. Chem. B* **2014**, *2*, 4398–4414.

(54) Hong, Y.; Lam, J. W. Y.; Tang, B. Z. Aggregation-Induced Emission. *Chem. Soc. Rev.* **2011**, *40*, 5361–5388.

TABLE OF CONTENTS GRAPHIC.